The Astrophysical Journal, 929:90 (11pp), 2022 April 10 https://doi.org/10.3847/1538-4357/ac5cb8

Surface Brightness Profile of Lyman-α Halos out to 320 kpc in HETDEX

Maja Lujan Niemeyer[1], Eiichiro Komatsu[1,2], Chris Byrohl[1], Dustin Davis[3], Maximilian Fabricius[4,5], Karl Gebhardt[3], Gary J. Hill[3,6], Lutz Wisotzki[7], William P. Bowman[8,9], Robin Ciardullo[8,9], Daniel J. Farrow[4,5], Steven L. Finkelstein[3], Eric Gawiser[10], Caryl Gronwall[8,9], Donghui Jeong[8,9], Martin Landriau[11], Chenxu Liu[3], Erin Mentuch Cooper[3,6], Masami Ouchi[2,12,13], Donald P. Schneider[8,9], and Gregory R. Zeimann[14]

[1] Max-Planck-Institut für Astrophysik, Karl-Schwarzschild-Straße 1, D-85741 Garching, Germany; maja@mpa-garching.mpg.de
[2] Kavli Institute for the Physics and Mathematics of the Universe (Kavli IPMU, WPI), University of Tokyo, Chiba 277-8582, Japan
[3] Department of Astronomy, The University of Texas at Austin, 2515 Speedway Boulevard, Austin, TX 78712, USA
[4] Max-Planck-Insitut für Extraterrestrische Physik, Giessenbachstraße, D-85748 Garching, Germany
[5] Universitäts-Sternwarte München, Scheinerstrasse 1, D-81679 München, Germany
[6] McDonald Observatory, The University of Texas at Austin, 2515 Speedway Boulevard, Austin, TX 78712, USA
[7] Leibniz-Institut für Astrophysik Potsdam (AIP), An der Sternwarte 16, D-14482 Potsdam, Germany
[8] Department of Astronomy & Astrophysics, The Pennsylvania State University, University Park, PA 16802, USA
[9] Institute for Gravitation and the Cosmos, The Pennsylvania State University, University Park, PA 16802, USA
[10] Rutgers, The State University of New Jersey, Piscataway, NJ 08854, USA
[11] Lawrence Berkeley National Laboratory, 1 Cyclotron Road, Berkeley, CA 94720, USA
[12] National Astronomical Observatory of Japan, 2-21-1 Osawa, Mitaka, Tokyo 181-8588, Japan
[13] Institute for Cosmic Ray Research, The University of Tokyo, 5-1-5 Kashiwanoha, Kashiwa, Chiba 277-8582, Japan
[14] Hobby-Eberly Telescope, University of Texas, Austin, Austin, TX, 78712, USA
Received 2021 November 30; revised 2022 February 18; accepted 2022 March 9; published 2022 April 15

Abstract

We present the median-stacked Lyman-α (Lyα) surface brightness profiles of 968 spectroscopically selected Lyα emitting galaxies (LAEs) at redshifts $1.9 < z < 3.5$ in the early data of the Hobby-Eberly Telescope Dark Energy Experiment. The selected LAEs are high-confidence Lyα detections with high signal-to-noise ratios observed with good seeing conditions (point-spread function FWHM $<1\farcs4$), excluding active galactic nuclei. The Lyα luminosities of the LAEs are $10^{42.4}$–10^{43} erg s^{-1}. We detect faint emission in the median-stacked radial profiles at the level of $(3.6 \pm 1.3) \times 10^{-20}$ erg s^{-1} cm^{-2} arcsec^{-2} from the surrounding Lyα halos out to $r \simeq 160$ kpc (physical). The shape of the median-stacked radial profile is consistent at $r < 80$ kpc with that of much fainter LAEs at $3 < z < 4$ observed with the Multi Unit Spectroscopic Explorer (MUSE), indicating that the median-stacked Lyα profiles have similar shapes at redshifts $2 < z < 4$ and across a factor of 10 in Lyα luminosity. While we agree with the results from the MUSE sample at $r < 80$ kpc, we extend the profile over a factor of two in radius. At $r > 80$ kpc, our profile is flatter than the MUSE model. The measured profile agrees at most radii with that of galaxies in the Byrohl et al. cosmological radiative transfer simulation at $z = 3$. This suggests that the surface brightness of a Lyα halo at $r \lesssim 100$ kpc is dominated by resonant scattering of Lyα photons from star-forming regions in the central galaxy, whereas at $r > 100$ kpc, it is dominated by photons from galaxies in surrounding dark matter halos.

Unified Astronomy Thesaurus concepts: Lyman-alpha galaxies (978); High-redshift galaxies (734); Circumgalactic medium (1879)

1. Introduction

Large Lyman-α (Lyα) emission regions with sizes of tens to hundreds of kiloparsec (kpc) were first found around high-redshift radio galaxies (McCarthy et al. 1987; van Ojik et al. 1997; Overzier et al. 2001; Reuland et al. 2003). Later, they were observed around quasars (Weidinger et al. 2004, 2005; Christensen et al. 2006; Goto et al. 2009; Smith et al. 2009; Cantalupo et al. 2014; Martin et al. 2014a, 2014b; Hennawi et al. 2015; Arrigoni Battaia et al. 2016; Borisova et al. 2016; Cai et al. 2018; Arrigoni Battaia et al. 2019a; Kikuta et al. 2019; Zhang et al. 2020), star-forming galaxies (Smith & Jarvis 2007; Smith et al. 2008; Shibuya et al. 2018), and in galaxy-overdense regions (Steidel et al. 2000; Matsuda et al. 2004; Yang et al. 2010; Matsuda et al. 2011; Cai et al. 2017). Measurements of the cross-correlation of Lyα intensity with quasar (Croft et al. 2016, 2018) or Lyα emitting galaxy (LAE) positions (Kakuma et al. 2021; Kikuchihara et al. 2021) revealed Lyα emission on even larger scales. Most individual high-redshift star-forming galaxies such as LAEs and Lyman-break galaxies (LBGs) are surrounded by smaller, 1–10 kpc size Lyα halos (Hayashino et al. 2004; Swinbank et al. 2007; Rauch et al. 2008; Ouchi et al. 2009; Patrício et al. 2016; Wisotzki et al. 2016; Leclercq et al. 2017; Smit et al. 2017; Erb et al. 2018; Claeyssens et al. 2019, 2022). Kusakabe et al. (2022) detected Lyα halos with sizes between 10 and 50 kpc in 17 out of 21 continuum-selected galaxies. While Bond et al. (2010), Feldmeier et al. (2013), and Jiang et al. (2013) report a lack of evidence for spatially extended Lyα emission around LAEs and LBGs, the ubiquitous presence of extended Lyα halos around high-redshift star-forming galaxies has been confirmed by stacking analyses (Møller & Warren 1998; Steidel et al. 2011; Matsuda et al. 2012; Momose et al. 2014, 2016; Xue et al. 2017; Wisotzki et al. 2018; Wu et al. 2020; Huang et al. 2021). The Multi Unit Spectroscopic Explorer (MUSE, Bacon et al. 2010) on the Very Large

Telescope (VLT) has revolutionized the subject by using up to 31 hour exposures to explore Lyα halos. By coadding a sample of 270 LAEs at $3 < z < 6$ in a 2 arcmin^2 section of sky, Wisotzki et al. (2018) found that Lyα emission can be traced out to several arcseconds from the source centers, so that nearly all the sky is covered by Lyα emission around high-redshift galaxies in projection.

The size of the Lyα halos around LAEs depends on their physical properties such as the ultraviolet (UV) and Lyα luminosities and the size of the UV-emitting region (Momose et al. 2016; Wisotzki et al. 2016; Leclercq et al. 2017; Xue et al. 2017). While Lyα halos are more compact in nearby galaxies than in high-redshift galaxies (e.g., Hayes et al. 2005; Östlin et al. 2009; Hayes et al. 2013, 2014; Leclercq et al. 2017; Rasekh et al. 2021), no significant redshift evolution of halos around LAEs within $2 < z < 6$ has been detected (Momose et al. 2014; Leclercq et al. 2017; Kikuchihara et al. 2021). In contrast, observed Lyα halo profiles of quasars are shown to increase from $z \sim 2$ to $z \sim 3$ and remain constant from $z \sim 3$ to $z \sim 6$ (Arrigoni Battaia et al. 2016, 2019a; Cai et al. 2019; Farina et al. 2019; O'Sullivan et al. 2020; Fossati et al. 2021).

There are various sources of Lyα photons that may contribute to the extended Lyα emission. One substantial source of Lyα photons is the local recombination of hydrogen atoms ionized by photons from young, massive stars in star-forming galaxies or from active galactic nuclei (AGN; Dijkstra 2019). Due to their resonant nature, Lyα photons are scattered by neutral hydrogen atoms in the circumgalactic medium (CGM) and the intergalactic medium (IGM). Lyα photons can also be created by collisional excitation, such as when dense gas flows into a galaxy (called "gravitational cooling"; Haiman et al. 2000; Fardal et al. 2001; Faucher-Giguère et al. 2010), and by fluorescence of hydrogen gas ionized by photons from more distant AGN or star-forming regions (called the "UV background"; Gould & Weinberg 1996; Cantalupo et al. 2005; Kollmeier et al. 2010; Mas-Ribas & Dijkstra 2016). Satellite galaxies can also contribute to the extended Lyα emission (Mas-Ribas et al. 2017).

In order to constrain the contributions of Lyα emission sources and mechanisms, it is necessary to model Lyα emission and its radiative transfer realistically. One method to model radiative transfer in Lyα halos is a perturbative approach (e.g., Kakiichi & Dijkstra 2018). Another way uses hydrodynamical simulations that resolve the gas around galaxies, which can be postprocessed with a Monte Carlo radiative transfer calculation to predict the shape of Lyα emission around galaxies (e.g., Lake et al. 2015; Kimock et al. 2021; Mitchell et al. 2021). Most of these models simulate small numbers of galaxies, while Zheng et al. (2011), Gronke & Bird (2017), and Byrohl et al. (2021) calculate Lyα radiative transfer in cosmological hydrodynamical simulations and offer predictions for large samples of galaxies. While being a promising tool, hydrodynamical simulations of galaxy formation in cosmological volumes with subkiloparsec resolutions (e.g., Nelson et al. 2020) possibly suffer from convergence issues both in the physical gas state (e.g., van de Voort et al. 2019) and in Lyα radiative transfer (e.g., Camps et al. 2021).

Comparisons of predictions with measurements draw different conclusions. While Steidel et al. (2011), Gronke & Bird (2017), and Byrohl et al. (2021) find that most of the extended Lyα emission can be explained by scattering of Lyα photons from the central galaxy or nearby galaxies, Lake et al. (2015) stressed the importance of cooling radiation in producing Lyα halos when they compared their simulation with observations from Momose et al. (2014). Mitchell et al. (2021) report that satellite galaxies are the predominant source of Lyα photons at 10–40 kpc, while cooling radiation also plays a relevant role.

Because the dominant origin of the Lyα halo photons depends on, among other things, the distance to the galaxies (Byrohl et al. 2021; Mitchell et al. 2021), observations of Lyα profiles out to larger distances will be helpful. An ideal data set for this is provided by the Hobby-Eberly Telescope Dark Energy Experiment (HETDEX; Hill et al. 2008; Gebhardt et al. 2021; Hill et al. 2021), which is designed to detect more than one million LAEs at redshifts $1.9 < z < 3.5$ in a 10.9 Gpc^3 volume to measure their clustering and thereby constrain cosmological parameters. HETDEX detects emission lines by simultaneously acquiring tens of thousands of spectra without any preselection of targets. In this work, we measure the median radial Lyα surface brightness profile of 968 LAEs at $1.9 < z < 3.5$ using the HETDEX data. We take advantage of the wide field of view of HETDEX and expand the measurement out to 320 kpc from the LAE centers.

This paper is structured as follows. Section 2 describes the data, the data processing, and the definition of the LAE sample. Section 3 presents the method for obtaining the median radial Lyα surface brightness profile of the LAEs and describes how we account for systematic errors. Section 4 reports the results and shows that simple stacking of the Lyα surface brightness profiles reproduces the rescaled best-fit model of stacked Lyα halos at higher redshift ($3 < z < 4$) at $r < 80$ kpc from Wisotzki et al. (2018). We quantify the effect of possible AGN contamination in the LAE sample by stacking sources with broad lines and high luminosities. In Section 5 we compare our results with theoretical predictions from a radiative transfer simulation by Byrohl et al. (2021) and from a perturbative approach by Kakiichi & Dijkstra (2018). We conclude in Section 6.

We assume a flat Λ cold dark matter (ΛCDM) cosmology consistent with the latest results from the Planck mission: $H_0 = 67.37$ km s^{-1} Mpc^{-1} and $\Omega_{m,0} = 0.3147$ (Planck Collaboration et al. 2020). All distances are in units of physical kpc/Mpc unless noted otherwise.

2. Data and Galaxy Sample

2.1. Data and Data Processing

We use spectra from the internal data release 2.1.3 (DR 2.1.3) of HETDEX, which were obtained with the Visible Integral-field Replicable Unit Spectrograph (VIRUS) on the 10 m Hobby-Eberly Telescope (HET; Ramsey et al. 1994; Hill et al. 2021). VIRUS consists of up to 78 integral-field unit fiber arrays (IFUs), each of which contains 448 1.″5 diameter fibers and spans $51'' \times 51''$ on the sky. The fibers from each IFU are fed to a low-resolution ($R = 800$) spectrograph unit containing two spectral channels, which covers the wavelengths between 3500 Å and 5500 Å. Each spectral channel has a CCD detector with two amplifiers; the spectra from the 448 fibers of each IFU are effectively split over four amplifiers. The IFUs with ~35k total fibers are distributed throughout the 18′ diameter of the telescope's field of view. Each HETDEX observation includes three 6-minute exposures, which are dithered to fill in gaps

between the fibers. The IFUs are arrayed on a grid with 100″ spacing. The gaps between the IFUs remain, so that the filling factor of one observation is $\sim 1/4.6$. Details of the upgraded HET and the VIRUS instrument can be found in Hill et al. (2021).

The data-processing pipeline is described in Gebhardt et al. (2021). A crucial aspect for detecting low surface brightness Lyα emission is the sky subtraction. HETDEX applies two separate approaches to sky subtraction, one using a local sky determined from a single amplifier (112 fibers spanning ~ 0.2 arcmin^2), and the other using a full-frame sky determined from the full array of IFUs (over 30k fibers).

For the local sky subtraction, we identify continuum sources by extracting a continuum estimate for each of the 112 fibers on a given amplifier using a wavelength range of 4100–5100 Å. We flag fibers with a $>3\sigma$ detection of continuum (using a biweight scale as σ; Beers et al. 1990) as continuum fibers. We further flag the two adjacent fibers in the spectroscopic image to each continuum fiber. This typically removes about 15% of the fibers. Of the remaining fibers, we apply a further cut of 10% of the fibers with the highest counts in the continuum region. The biweight location, which is a robust estimate of the central location of a distribution (Beers et al. 1990), of the remaining approximately 75% of the fibers determines the local sky spectrum. There is residual low-level background that is due to a combination of dark current, scattered light, mismatch of the fiber profile, and illumination differences for the specific exposure. After removing the identified continuum sources, we smooth the spectroscopic image with a two-dimensional biweight filter that is six fibers by 700 Å across in order to estimate and remove the broad-scale residual background (background light correction). This procedure is highly effective at removing the residual background at the expense of removing some continuum of faint sources. While this local sky subtraction is robust, extended emission that covers a significant fraction of the small area of an amplifier can be mistaken as sky emission and thus removed from the signal.

As an alternative, HETDEX provides a full-frame sky subtraction. This procedure uses over 30k fibers, which provides a significant improvement for objects that dominate an amplifier. Continuum sources are identified in the same manner as the local sky estimate. The disadvantage of this procedure is that the amplifiers have individual differences that need to be addressed. These include differences in the illumination of the primary mirror on the IFUs across the 20′ field, the wavelength solution, and the instrumental dispersion.

There are two components to the amplifier-to-amplifier normalization for the full-frame sky spectrum. The first component is the instrumental throughput difference that we measure from the twilight frames. The second is due to the different illumination patterns of the primary as the HET tracks a specific field, leading to illumination differences of the IFUs. We use the relative residual flux in the sky-subtracted images to determine the relative normalizations due to illumination. Because there is a broad wavelength dependence, we use a low-order term to adjust the normalization for each amplifier coming from four wavelength regions averaged over 500 Å regions. The scalings range from 0.9 to 1.1, and we use deviations beyond this range as a flag for data that potentially have to be removed due to detector controller issues. The wavelength dependence is small, generally below 1%. Because the local sky subtraction uses one sky spectrum for each amplifier, the illumination differences are irrelevant.

The other important aspect is due to small changes in the wavelength solution. We use the full-frame sky wavelength solution to adjust the local values. During the full-frame sky subtraction, we allow each amplifier to fit for a wavelength offset and a dispersion term. The offsets are generally small (smaller than 0.2 Å), but the dispersion term can be more important. We think that the dispersion term is caused by differential breathing modes in the spectrograph due to temperature changes. For the majority of amplifiers, the sky-subtracted frames from the full frame and local sky look very similar. In a few, the dispersion term does not adequately capture the changes in the wavelength solution, causing small residuals correlated with bright sky lines. The background residual counts within a given amplifier still need to be removed, which will subtract some light from the faintest sources. We are confident that while some uncertainty in the background estimate remains, the line flux relative to the continuum is unaffected.

One aspect we do not account for are changes in instrumental resolution across spectrographs. While we have built these to have a resolving power as uniform as possible, there are differences. In particular, the resolution can change across the amplifier, where fibers at the edge of spectrographs have a larger instrumental dispersion. The local sky subtraction naturally deals with the variation from spectrograph to spectrograph, but the full-frame does not. The variation within a spectrograph is equally a problem in both sky subtraction procedures. We do not address these differences at this point. The effect is small and only noticeable at some of the edges of spectrographs. To compensate for these issues, our noise model takes into account the larger residuals and increases the noise at these locations. Less than 5% of the fibers are affected by this increased noise.

The full-frame sky subtraction over the large field of view of VIRUS offers an advantage for extended objects over the local sky subtraction and over instruments such as MUSE, which has a smaller field of view with which to measure the sky spectrum. We therefore adopt the full-frame sky subtraction.

2.2. LAE Sample

We draw our sample of LAEs from the line emission catalog from the HETDEX internal DR 2 (specifically, v2.1.3) to be published in Mentuch Cooper et al. (2022, in preparation), which contains approximately 300k LAEs. For each detected line, the catalog provides the coordinates of the centroid, the central wavelength, the line width, the line flux, the signal-to-noise ratio (S/N), and the probability of the feature being a Lyα line. This probability is computed by the HETDEX Emission Line eXplorer (ELiXer; D. Davis et al., 2022, in preparation), which uses multiple techniques including a Bayesian Lyα-versus-[O II] λ3727 discrimination (Leung et al. 2017; Farrow et al. 2021). To minimize contamination of nearby objects and artifacts, the ELiXer probability P(Lyα) of every line in our sample must be higher than 0.9 (the minimum $P(\mathrm{Ly}\alpha)/P([\mathrm{O\,II}])$ is 9).

We require that the lines have an S/N $\geqslant 6.5$ to minimize false-positive detections. The minimum throughput at 4540 Å of an observation must be >0.08 for HETDEX to include its line detections in the catalog. In this work, we only include LAEs in observations with throughput >0.13 and good seeing

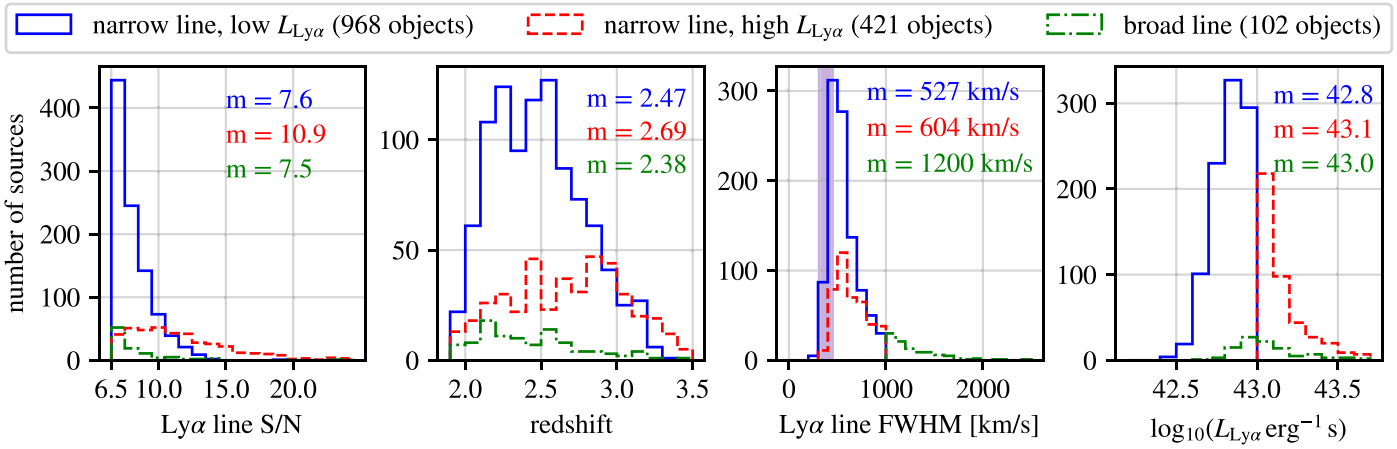

Figure 1. Distributions and median values (m) of several properties of the sources in the three samples: NLLL sources are shown in solid blue, NLHL sources are shown in dashed red, and BL sources are shown in dot–dashed green. The first panel presents the S/N distributions for S/N $\geqslant$ 6.5. The second panel displays the redshift distributions. The third panel shows the Lyα-line FWHM. The purple shaded area shows the instrumental resolution over the redshift range of the instrument (5.6Å; Hill et al. 2021). The NL and BL samples are separated at $\mathrm{FWHM}_{Ly\alpha} = 1000\ \mathrm{km\ s^{-1}}$. The fourth panel shows the Lyα luminosity. Because of the high S/N requirement, the sources have luminosities $>10^{42.4}\ \mathrm{erg\ s^{-1}}$. The LL and HL samples are divided at $L_{Ly\alpha} = 10^{43}\ \mathrm{erg\ s^{-1}}$.

(point-spread function, PSF, FWHM $< 1\farcs4$) to resolve the Lyα halos. Furthermore, we only use observations that were taken in 2019 and later, as earlier data had more detector artifacts and often larger sky emission residuals.

After visually inspecting the remaining sources and excluding non-LAEs, our sample consists of 1491 high-confidence high-redshift Lyα emitting objects that are detected in 150 observations.

This initial sample contains AGN. Since we are interested in the Lyα halos of LAEs without an AGN, we divide the sample into three subgroups. The first criterion is the line width: galaxies with a Lyα line $\mathrm{FWHM}_{Ly\alpha} \geqslant 1000\ \mathrm{km\ s^{-1}}$ are placed into the broad-line sample (BL, 102 objects). The remaining sources are separated by their luminosity: galaxies with a Lyα luminosity $L_{Ly\alpha} \geqslant 10^{43}\ \mathrm{erg\ s^{-1}}$ constitute the narrow-line, high-luminosity sample (NLHL, 421 objects), and galaxies with $L_{Ly\alpha} < 10^{43}\ \mathrm{erg\ s^{-1}}$ constitute the narrow-line, low-luminosity sample (NLLL, 968 objects). We use the NLLL subset as our final LAE sample. The luminosity threshold represents the luminosity at which narrow-band selected LAEs start to be dominated by AGN (Spinoso et al. 2020). Zhang et al. (2021) find that the AGN fraction at $2.0 < z < 3.5$ at $L_{Ly\alpha} < 10^{43}\ \mathrm{erg\ s^{-1}}$ is <0.05; hence this is a conservative threshold. In this fashion, we remove most AGN from the NLLL/LAE sample. We compare the median radial profile of the LAE sample to those of the other two samples to study the impact of potential AGN contamination.

Figure 1 shows the distributions of S/N, redshift, Lyα-line FWHM, and Lyα luminosities of the NLLL (blue), the NLHL (red), and the BL (green) samples. Figure 2 displays the median spectrum of the NLLL/LAEs in the rest frame without continuum subtraction. We interpolate the spectra of the closest fiber to each LAE on a rest-frame wavelength grid with a bin size of 0.4 Å. Then we take the median of the individual LAE spectra.

The median spectrum possesses continuum, a prominent Lyα line (1216 Å), and a faint C IV line (1550 Å). The large observed Lyα equivalent width ($\mathrm{EW}_{Ly\alpha} = 96 \pm 3$ Å) indicates that the LAE sample mainly consists of Lyα emitting galaxies, rather than low-z [O II] galaxies (Ciardullo et al. 2013; Santos et al. 2020). The strength of the C IV emission

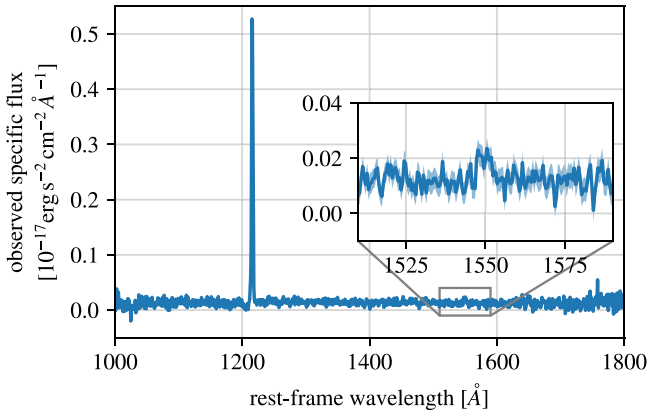

Figure 2. Median spectrum of the 968 LAEs in the NLLL sample in the rest frame. We use the original, not continuum-subtracted, spectrum of the fiber closest to each LAE. The observed specific flux is interpolated on a regular rest-frame wavelength grid with 0.4 Å binning to obtain the median spectrum. The inset shows the C IV emission line ($\mathrm{EW}_{\mathrm{Civ}} = 4.0 \pm 0.7$ Å).

($\mathrm{EW}_{\mathrm{Civ}} = 4.0 \pm 0.7$ Å) is consistent with predictions for star-forming galaxies (Nakajima et al. 2018). It is also within the range reported by Feltre et al. (2020), who studied the mean rest-frame UV spectra of LAEs at $2.9 < z < 4.6$ using MUSE. Our NLHL sample has a similar Lyα equivalent width ($\mathrm{EW}_{Ly\alpha} = 94 \pm 3$ Å) and C IV emission ($\mathrm{EW}_{\mathrm{Civ}} = 3.4 \pm 0.7$ Å). Our BL sample has a similar Lyα equivalent width ($\mathrm{EW}_{Ly\alpha} = 103 \pm 7$ Å), but larger C IV emission ($\mathrm{EW}_{\mathrm{Civ}} = 5.5 \pm 1.5$ Å), as expected for a larger fraction of AGN in the sample. The N V (1239 Å and 1243 Å) and Si IV (1394 Å and 1403 Å) emission lines are not detected in median spectra of the NLLL, NLHL, or BL samples. The median spectra of the NLLL and NLHL samples have a He II (1640 Å) equivalent width of 2.2 ± 0.6 Å, which is consistent with that of bright ($L_{Ly\alpha} > 10^{42.05}\ \mathrm{erg\ s^{-1}}$) LAEs reported by Feltre et al. (2020).

2.3. Masking and Continuum Subtraction

We mask the wavelength regions around bright sky lines to avoid the largest sky emission residuals.

To isolate the Lyα emission, we remove continuum emission of the LAEs from the spectra. In each fiber, we subtract the median flux within 40 Å of the Lyα line center, but excluding the central 5 $\sigma_{\mathrm{Ly}\alpha}$, where $\sigma_{\mathrm{Ly}\alpha}$ is a Gaussian σ from the fit to the emission line. Subtracting only the continuum on the red side of the Lyα line or changing the excluded central window from $5\sigma_{\mathrm{Ly}\alpha}$ to $7\sigma_{\mathrm{Ly}\alpha}$ does not affect our results. We subtract the continuum emission of all fibers instead of masking those with high continuum emission for multiple reasons. Most importantly, the resulting surface brightness profiles have insignificant differences because the continuum subtraction successfully removes the continuum flux from projected neighbors. It is also difficult to mask continuum sources completely because of the large PSF of VIRUS. In the masking scheme, many fibers in the core of our LAE sample were masked. Finally, the continuum subtraction removes the systematic effect from an incorrect background subtraction, which can add a constant or smooth wavelength-dependent flux to each spectrum.

3. Detection of Lyα Halos

3.1. Extraction of Lyα Surface Brightness

We integrate the flux density over the wavelengths around the Lyα line of each LAE to obtain a surface brightness for each fiber that is located within 320 kpc of the LAE (typically 1100 fibers). The width of this integration window is different for each LAE and is chosen to be three times the $\sigma_{\mathrm{Ly}\alpha}$ of the Gaussian fit to the Lyα emission line. The integration-window widths range from 5 Å to 18 Å (NLLL sample) in the observed reference frame, with a median (mean) of 10 Å (12 Å). To investigate the influence of the variable width on the radial profile measurement, the measurement was repeated with a fixed width of $\Delta\lambda = 11$ Å; the results are consistent with one another. We choose the variable-width approach because the results have a slightly higher S/N.

The result of this preparation is a set of surface brightness values as a function of angular separation from the centroid of each LAE. We translate this angular distance into a physical distance assuming our fiducial cosmology and sort the fibers around each LAE by their distance from it.

3.2. Stacking

We take the median surface brightness of all fibers around all LAEs in radial bins. The bin edges are at 5, 10, 15, 20, 25, 30, 40, 60, 80, 160, and 320 kpc. In each bin, we gather all fibers whose distance from the fiber center to their corresponding LAE lies within this range. We do not normalize the surface brightness of the fibers around each LAE in order to retain physical units. We take the median surface brightness of these fibers and use a bootstrap algorithm to determine the uncertainty. Each bin contains fibers from at least 55% of the LAEs in the NLLL sample, and at $r > 10$ kpc, more than 96% of the LAEs contribute to each bin.

3.3. Estimating Systematic Uncertainty

We explore the systematic uncertainty in two steps. The first part addresses the median surface brightness that would be interpreted as extended Lyα emission in random locations on the sky rather than centered on an LAE, which we refer to as the background surface brightness. One total value is used for this quantity, which is the sum of contributions from Lyα emission in the target redshift, other redshifted emission lines, continuum emission from stars and nearby galaxies, and sky emission residuals. To measure this background surface brightness, we repeat our surface brightness measurements at random locations. Specifically, for each LAE we randomly draw a fiber within the same observation and choose a random location within 1″ of this fiber as the centroid. To avoid the possibility that any of the LAE halo Lyα affect our experiment, we require that this new position be farther away than 2′ from the original LAE. These random locations may coincide with foreground objects. This is intentional because we probe the Lyα halos out to >30″, which can include foreground objects. It is therefore appropriate not to exclude these from the random sample. We then integrate the flux of the fibers within 20″ of this location over the same wavelengths used for the integration of the real LAE. For each LAE, we generate three of these random measurements, producing a data set for comparison that has the same distribution of wavelengths and widths of integration windows as the LAE, but is centered on random, but not necessarily empty, sky positions. Because we prepare the spectra identically to those around LAEs, this background estimate accounts for potential systematic effects introduced by the continuum subtraction.

We use the median of our random position measurements to estimate the background surface brightness and a bootstrap algorithm to estimate the uncertainty. We find $(4.0 \pm 0.4) \times 10^{-20}$ erg s^{-1} cm^{-2} arcsec^{-2} for the NLLL sample. The nonzero background does not contradict the efficacy of the full-frame sky subtraction. It can be caused, for example, by the complicated asymmetric shape of the pixel flux distribution, nonflat fiber spectra, and differences in averaging estimators.

Having considered systematic uncertainties derived on larger volumes, we now address systematic errors associated with proximity of the LAEs. This second step largely follows the procedure of Wisotzki et al. (2018). For each LAE, we repeat the surface brightness extraction, but shift the central wavelength in increments of 10 Å from the observed Lyα wavelength, where the minimum offset is 20 Å and the maximum offset is 210 Å. This produces 40 sets of Lyα-free pseudo-narrow-band images for each LAE, which we then combine to make 40 Lyα-free stacks, each separated by $\Delta\lambda$. Their standard deviation is then defined as the empirical uncertainty of the stack of LAEs. The median ratio of these empirical errors to the statistical error using the bootstrap algorithm is 1.5. We adopt the larger of the two error estimates as the uncertainty of the median surface brightness in each bin. The median of the wavelength-shifted profiles is consistent with the background at $r > 50$ kpc.

We subtract the background surface brightness to find the median Lyα surface brightness profile around our LAE sample. Since the random sample depends on the sample of sources, the BL, NLHL, and NLLL samples each have one background surface brightness. The uncertainty of the background estimate is included in the uncertainty of the final Lyα surface brightness profile via Gaussian error propagation.

We can compare the reported errors to the propagation of errors from an individual fiber, which we expect to be smaller. The average flux uncertainty on an individual fiber is $\sim 7 \times 10^{-18}$ erg s^{-1} cm^{-2} within 10 Å, which is the average integration width of the LAEs. Taking into account the fiber area and the number of fibers going into each bin, we can

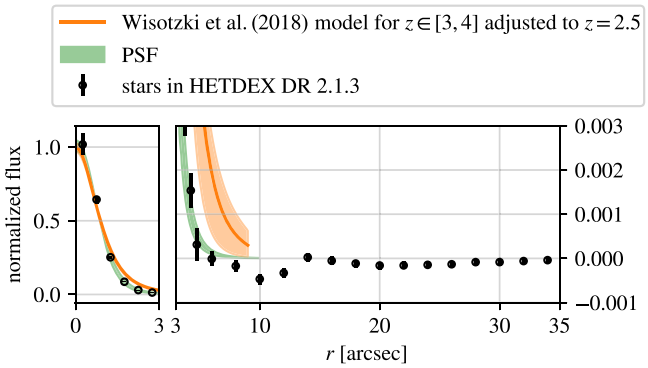

Figure 3. Normalized median radial profile of 3795 stars in our observations (black points) compared to the PSF model (green). The model is a Moffat function with $\beta = 3$ and $1\farcs2 \leqslant \mathrm{FWHM} \leqslant 1\farcs4$. The orange shaded area is the best-fit model from Wisotzki et al. (2018) for Lyα halos at $3 < z < 4$ adjusted to our observation and normalized. The right panel is a continuation of the left panel in radius, but covering a smaller range in flux. The radial profile of the stars is negative at $r \gtrsim 5''$ because of small errors in the background light correction.

estimate the surface brightness limit for each bin. For example, at 120 kpc, we have 3×10^5 fibers, each with $1\farcs5$ diameter, which gives a surface brightness uncertainty of 7×10^{-21} erg s^{-1} cm^{-2} arcsec^{-2}. Our measured uncertainty is 1.3×10^{-20} erg s^{-1} cm^{-2} arcsec^{-2}. The larger uncertainties are due to a combination of the intrinsic differences of LAEs and our attempt to include systematic effects.

3.4. Shape of the Point-Spread Function

Multiple independent techniques show that the PSF of VIRUS is well modeled by a Moffat function with $\beta \in [3, 3.5]$ in good seeing conditions (Gebhardt et al. 2021; Hill et al. 2021). To test this, we measure the median radial profile of Gaia stars observed by VIRUS in the same observations as the LAEs. We select 3795 faint stars (g-band magnitude between 19 and 20) from the Gaia DR1 catalog (Gaia Collaboration et al. 2016). For each fiber close to the centroid of the star, we compute the weighted mean flux density within $4550\,\mathrm{Å} < \lambda < 4650\,\mathrm{Å}$, where the weights are the inverse squared flux density errors. We use the spectra without continuum subtraction for the stars because their spectra mostly consist of continuum emission. The radial profiles of the stars are stacked by taking the median in radial bins.

Figure 3 shows the stacked radial profile of the stars compared to the PSF model with $\beta = 3$. The exact choice of β does not affect our results. While the profile traces the PSF shape well at $r \lesssim 5''$, the median flux at larger radii is mostly negative. We suspect that this behavior is due to an overestimating of the sky from undetected background galaxies. We correct this effect for the LAEs by using the continuum-subtracted spectra and by subtracting the background surface brightness.

4. Results

The left panel of Figure 4 displays the median Lyα surface brightness profile around our set of LAEs (blue; NLLL sample). The PSF in our observations is shown as a comparison. This median Lyα surface brightness profile is clearly more extended than the profile of a point source and shows significant emission of $(3.6 \pm 1.3) \times 10^{-20}$ erg s^{-1} cm^{-2} arcsec^{-2} out to 160 kpc. The median profile of continuum emission at longer wavelengths than Lyα is consistent with the PSF, but it has an insufficient S/N for a meaningful comparison.

The right panel of Figure 4 shows the comparison of the median radial profiles of the three samples: the LAE/NLLL sample (blue), the NLHL sample (red), and the BL sample (green). The NL samples have similar shapes, while the BL sample is flatter at intermediate radii ($25\,\mathrm{kpc} \leqslant r \leqslant 60\,\mathrm{kpc}$). Both the NLHL and the BL samples have a higher overall surface brightness than the LAE/NLLL sample, suggesting that the effect of potential AGN contamination in the LAE sample is a higher overall surface brightness and possibly a flattening of the radial profile at intermediate radii. For example, the stacked surface brightness profile of 15 quasars at $z \sim 2$ obtained from narrow-band images yields $(5.5 \pm 3.1) \times 10^{-20}$ erg s^{-1} cm^{-2} arcsec^{-2} in a large radial bin of $50 < r < 500\,\mathrm{kpc}$ (Arrigoni Battaia et al. 2016). While the statistical significance is low, this level of surface brightness is consistent with that of our NLHL sample.

The left panel of Figure 4 compares the profile to the best-fit model for the stack of LAEs at $3 < z < 4$ reported in Wisotzki et al. (2018). This model consists of a point-like profile proportional to the PSF plus a halo profile following a Sérsic function. The point-like contribution has a total flux $F_{\mathrm{ps}} = (232 \pm 50) \times 10^{-20}$ erg s^{-1} cm^{-2} and FWHM $= 0.703''$ for the MUSE instrument. The Sérsic function has a total flux $F_{\mathrm{h}} = (1488 \pm 83) \times 10^{-20}$ erg s^{-1} cm^{-2}, effective radius $r_{\mathrm{eff,h}} = 0\farcs86 \pm 0\farcs11$, and Sérsic index $n_{\mathrm{h}} = 2.8 \pm 1.1$.

Before we compare this model with our data, we have to account for several differences between the two data sets. First, our LAE sample is located at lower redshifts ($1.9 < z < 3.5$) and it is on average much brighter (by a factor of 10 in Lyα luminosity) in Lyα than the LAE sample of Wisotzki et al. (2018). Second, VIRUS has a larger PSF and larger fiber diameter than MUSE. To account for the redshift difference, we translate the angular separation at $z_{\mathrm{mid}}^{\mathrm{MUSE}} = 3.5$ into physical distances and back to the corresponding angular separation at our median redshift $z_{\mathrm{median}} = 2.5$ (10% change in scale). We then convolve the model profile with the median PSF of our observations, i.e., a Moffat function with $\beta = 3$ and FWHM $= 1\farcs3$. Because the fibers on VIRUS are larger, we also convolve the model profile with the fiber face (a top-hat with radius $0\farcs75$). As our sample of galaxies is brighter, we multiply the model profile by 10.3 such that the flux in the core ($r \leqslant 2''$) of our measured radial profile and the model match.

The adjusted model agrees qualitatively well with our measured radial profile at $r < 80$ kpc despite the differences in redshift and Lyα luminosities of the LAE samples. At larger radii, our radial profile becomes flatter than the model. However, the measured radial profile from Wisotzki et al. (2018) is also above the fitted profile by 2 σ at 60 kpc, which is consistent with a flatter outer radial profile.

There are three possible reasons for the discrepancy at larger radii. First, an unknown systematic error in our analysis may artificially flatten the radial profile. Second, the smaller field of view of MUSE may cause them to oversubtract extended Lyα emission and thereby miss the flattening. Third, the flattening may depend on the Lyα luminosity or redshift of the LAE sample and may be stronger for brighter, probably more massive LAEs at lower redshift. To test the second possible reason, we imitate a background subtraction for each VIRUS IFU, which is slightly smaller than the MUSE field of view. This removes the flattening at $r \geqslant 50$ kpc. To investigate

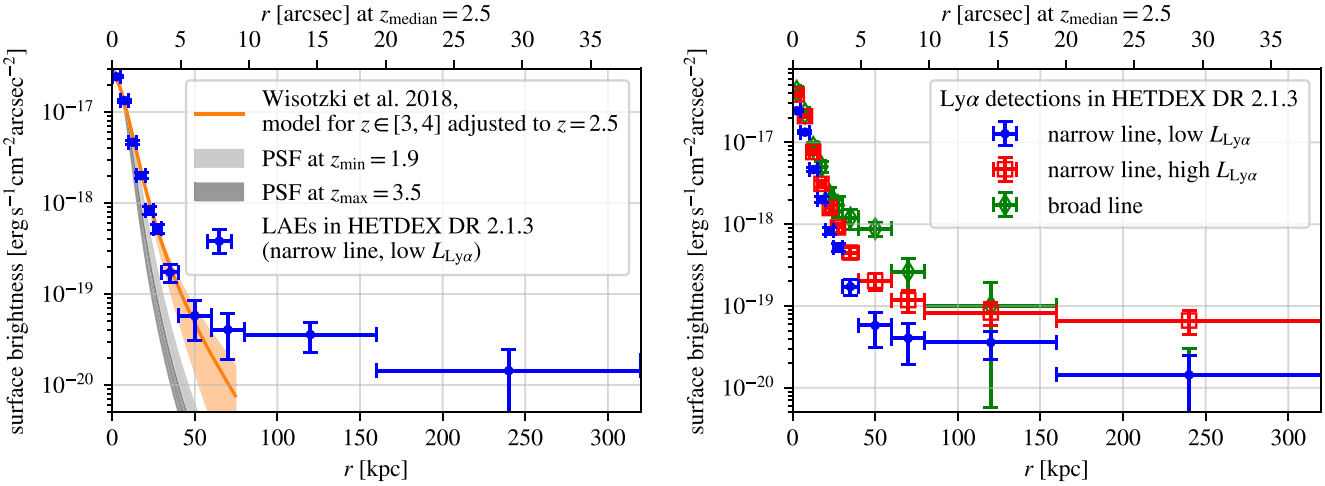

Figure 4. Left: median Lyα surface brightness profile of our LAE sample (blue; FWHM$_{Ly\alpha} < 1000$ km s^{-1} and $L_{Ly\alpha} < 10^{43}$ erg s^{-1}) after subtracting the background surface brightness. The gray shaded area shows the PSF in the observations at the minimum and maximum redshift. The orange profile is the best-fit model in Wisotzki et al. (2018) for LAEs at $3 < z < 4$, adjusted to our observations and rescaled to match the flux of our galaxies in the core. Our measured radial profile agrees well with this model within 80 kpc, but is flatter at larger radii. Right: comparison of the median Lyα surface brightness profile of the LAE sample (blue) to those with broad lines (green diamonds) and narrow lines and high luminosities (red squares). The background surface brightness values of each sample have been subtracted.

a possible luminosity dependence, future studies can expand this analysis to fainter LAEs in HETDEX data. The redshift dependence can be tested by expanding the LAE sample and splitting it into redshift bins.

5. Discussion

5.1. Impact of the Background Subtraction

The main goal of this paper is to measure the shape of the Lyα emission around LAEs, which requires the removal of background emission. We subtract background emission in three steps: the sky subtraction (Section 2.1), the continuum subtraction (Section 2.3), and the subtraction of the remaining background surface brightness (Section 3.3). The sky subtraction removes the (biweight) average flux within 18′, which covers 8–9 Mpc in our redshift range, in each 2 Å wavelength bin. The continuum subtraction removes the median flux within $\Delta\lambda = 80$ Å in the observed frame, which corresponds to a line-of-sight distance of 12–36 Mpc, of each fiber. The background subtraction removes the median surface brightness of random locations within 18′ or 8–9 Mpc with the same wavelength and integration-window distribution as the LAEs.

It is difficult to disentangle contributions from sky emission residuals, astronomical foreground objects, and the genuine diffuse Lyα background to the subtracted background estimates. Due to these background subtraction procedures, we may therefore underestimate the Lyα surface brightness. The affected scale is ∼10 Mpc, which is almost two orders of magnitude larger than our observed range of the Lyα profiles. Hence the uncertainty of the background Lyα surface brightness should manifest itself as a constant additive term and does not affect the shape of the Lyα profiles.

5.2. Comparison with Theoretical Predictions

Figure 5 compares the median radial profile of the NLLL LAE sample with the prediction for Lyα halos from the simulation in Byrohl et al. (2021) at $z = 3$. The surface brightness of the simulated Lyα halos is integrated over 2.2 Mpc wide slices along the line of sight. This approach is

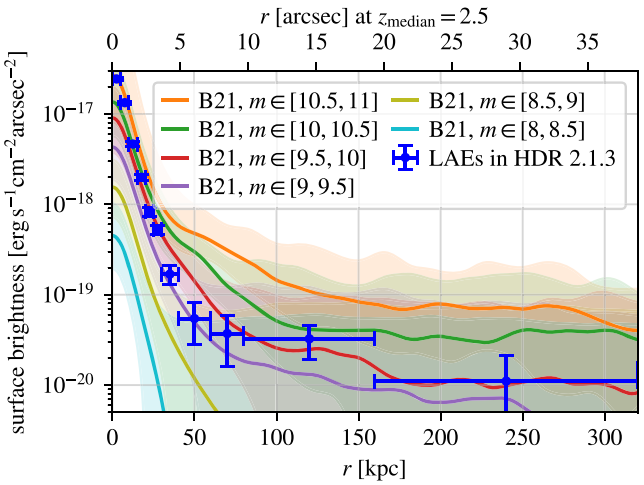

Figure 5. Median Lyα surface brightness of the NLLL LAE sample (blue) after subtracting the background, compared to the median simulated surface brightness profiles in Byrohl et al. (2021) in six stellar mass bins ($m = \log_{10}(M_\star/M_\odot)$), adjusted to our observations.

similar to the integration width of our measurement, which has a median (mean) of 2.7 Mpc (2.9 Mpc). To adjust the radial profile from the simulation to our observations, we convolve it with the median PSF and VIRUS fiber face. We then subtract the mean Lyα surface brightness in the entire simulation volume (1.9×10^{-20} erg s^{-1} cm^{-2} arcsec^{-2}) from the simulated radial profiles to emulate the background subtraction in our data analysis. Finally, we multiply the profiles by $(1+3)^4/(1+2.5)^4 \approx 1.7$ to account for surface brightness dimming.

This figure displays the median radial profiles of simulated galaxies in six stellar mass ranges between 10^8 and $10^{11} M_\odot$. Our measurements are consistent with the simulated ones; in detail, however, our measured Lyα surface brightness profile is steeper than the profiles from the simulation at $r \lesssim 50$ kpc.

The Byrohl et al. (2021) simulation finds that most photons illuminating Lyα halos originate from star-forming regions within the central galaxy or, at large radii, nearby galaxies,

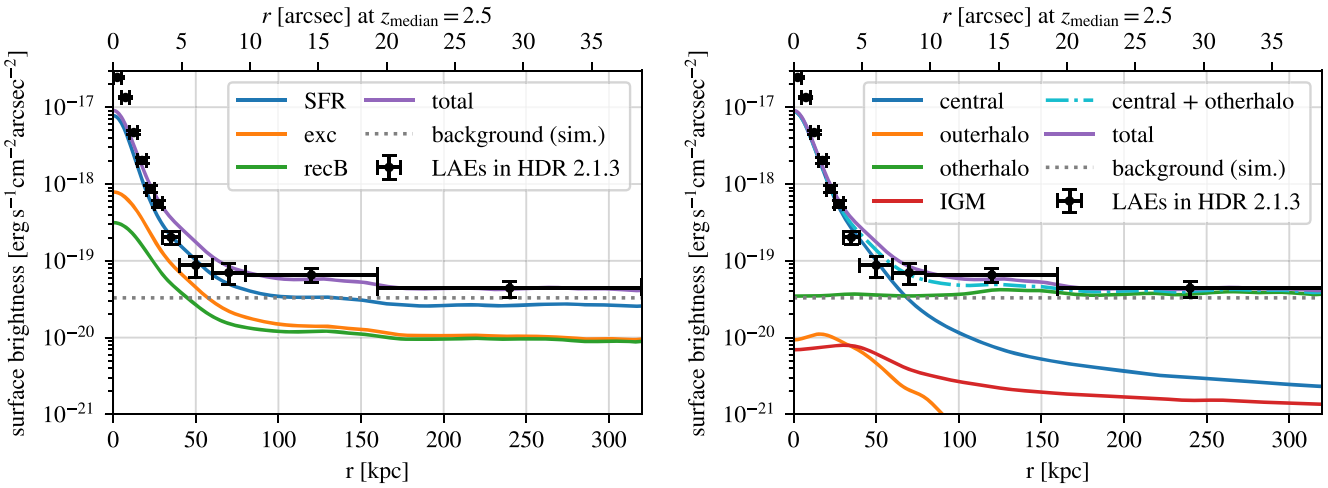

Figure 6. Median Lyα surface brightness profile of the NLLL/LAE sample in HETDEX (black) compared to the median surface brightness profiles of simulated galaxies with stellar masses $M_\star \in [10^{9.5} M_\odot, 10^{10} M_\odot]$ from Byrohl et al. (2021). The dashed gray line indicates the mean Lyα surface brightness of the simulation (background (sim.)), which we add to the measured Lyα surface brightness profile. Left: different emission mechanisms of the Lyα photons: recombination after photoionization from star formation (SFR; blue), collisional excitation (exc; orange), case-B recombination after including photoionization from an ionizing background (recB; green), and the sum of these (total; purple). The SFR dominates the simulated profile at all radii. Right: different emission origins of the Lyα photons: the central galaxy in the target dark matter halo (central; blue), the outer parts of this dark matter halo (outerhalo; orange), another dark matter halo than the target halo (otherhalo; green), IGM (red), and the sum of these (total; purple). The sum of the central and otherhalo contributions (cyan dot–dashed line) reproduces the measured surface brightness profile well except in the core ($r < 10$ kpc).

which are scattered in the CGM/IGM. Other emission mechanisms and emission origins contribute less to the total median Lyα profile. Figure 6 compares the measured surface brightness profile with the median profiles of individual emission mechanisms and emission origins from simulated galaxies with $M_\star \in [10^{9.5} M_\odot, 10^{10} M_\odot]$. For an informative comparison, the mean Lya surface brightness from the simulation ("background (sim.)") is added to the measured profile because the mean surface brightness for individual simulated components was not available.

The left panel shows different emission mechanisms. The SFR dominates the simulated surface brightness profile at all radii.

The right panel presents different emission origins before the scattering of the Lyα photons. The sum of the central component and the otherhalo component is close to the measured surface brightness profile, suggesting that photons originating from the outer parts of the dark matter halo and IGM play only a minor role in forming the total profile.

While the level of agreement is impressive, there are small discrepancies. One reason is linked to modeling limitations in the hydrodynamic simulations and their Lyα radiative transfer treatment: the lack of coupled ionizing radiation from star-forming regions, the lack of dust modeling, and uncertainty in the intrinsic Lyα luminosities within galaxies.

The Lyα radiation escaping from the ISM is largely determined by the complex radiative transfer in the ISM multiphase state that remains unresolved in the simulation. Along with large uncertainties on the intrinsic Lyα luminosity of stellar populations and potential Lyα emission from obscured AGN, large uncertainties for the Lyα luminosity escaping the ISM exist. The assumed linear scaling between star formation rate and ISM-escaping Lyα luminosity in Byrohl et al. (2021) may not accurately reflect reality. The observations reveal substantial scatter in the scaling relation (Runnholm et al. 2020; Santos et al. 2020). The selection of the galaxies in the observation is also different than in the simulation. We may therefore not reflect a potential bias for the observational sample regarding their star formation and dust content. Finally, while the simulation uses the mean to convert two-dimensional images into radial profiles, we use the median.

In addition to the comparison to hydrodynamical simulations, we also consider an analytically motivated approach by Kakiichi & Dijkstra (2018), who predict a Lyα radial profile following a power law $\propto r^{-2.4}$ for $r \in [20,\ 1000]$ kpc. In this approach, only scatterings of photons from the central galaxy in the CGM are considered. We compare this prediction with our measurement by fitting a similar model to our stack. The model consists of a point-like component given by a δ function times a constant a, plus a power-law halo, which we terminate at $r_0 = 1''$ ($\approx$8 kpc) to avoid divergence at smaller radii. The profile is therefore given by

$$f(r, \phi) = a \times \delta(r) + b \times \begin{cases} 1 & \text{if } r < 1'' \\ \left(\frac{r}{''}\right)^{-2.4} & \text{if } r \geqslant 1''. \end{cases} \quad (1)$$

We convolve the profile at the median redshift ($z_{\rm median} = 2.5$) with the PSF and VIRUS fiber face and fit to the data by varying the constants a and b.

Figure 7 shows the result. The power-law fit agrees well with the data out to $r = 80$ kpc. At larger radii, it underestimates the Lyα surface brightness. Because the model only considers scattering of Lyα photons originating from the central galaxy, the flattening of the profile at large radii ($r \gtrsim 100$ kpc) may be caused by photons that originate from other dark matter halos, as predicted by Byrohl et al. (2021). The outer surface brightness profile is also consistent with the results of Mas-Ribas & Dijkstra (2016) using the CGM model of Dijkstra & Kramer (2012), further suggesting that the clustering of ionizing sources around the LAEs is an important factor.

Another reason for the flattening of the Lyα profile may be fluorescence from the ultraviolet background. The values predicted by Cantalupo et al. (2005) and Gallego et al. (2018, 2021) are on the order of 10^{-20} erg s^{-1} cm^{-2} arcsec^{-2} at $z \sim 3$, which is consistent with the simulations of Byrohl et al.

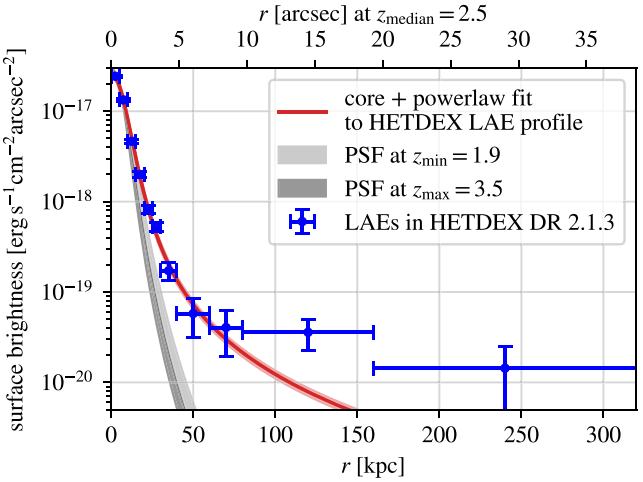

Figure 7. Median Lyα surface brightness of the NLLL LAE sample (blue) after subtracting the background. The gray shaded area represents the PSF in the observations at the minimum and maximum redshift. The red line is the least-squares fit of a "core plus power-law" profile motivated by Kakiichi & Dijkstra (2018). The red shaded area shows the 1σ uncertainty of the least-squares fit.

(2021) and the outermost points of our observed profile, but insufficient to explain the surface brightness at intermediate radii. Recent observations hint at the detection of the filamentary structure of the cosmic web traced by Lyα at a surface brightness $\sim 10^{-20}$–10^{-18} erg s^{-1} cm^{-2} arcsec^{-2} at $z \sim 3$ in overdense regions (Arrigoni Battaia et al. 2019b; Umehata et al. 2019; Bacon et al. 2021). Because of their rarity and small volume, they may contribute to but are unlikely to dominate the median-stacked profile on large scales. Future multidimensional analysis similar to Leclercq et al. (2020) can give additional insights on the nature of the extended emission and its link to the Lyα-emitting cosmic web.

Finally, satellite galaxies or galaxies within the integration window of the Lyα line along the line of sight may contribute to the extended Lyα emission (Mas-Ribas et al. 2017).

6. Summary

We presented the median radial Lyα surface brightness profile of 968 LAEs at $1.9 < z < 3.5$ that were carefully selected from the DR 2.1.3 of the HETDEX survey. The presence of Lyα halos is detected at $(3.6 \pm 1.3) \times 10^{-20}$ erg s^{-1} cm^{-2} arcsec^{-2} out to 160 kpc. The potential residual AGN contamination in the LAE sample may increase the overall amplitude of the median radial profile and may flatten the profile in the intermediate radii.

We compared the radial profile with the rescaled model of Wisotzki et al. (2018) for the median radial profile of fainter LAEs at $3 < z < 4$, which we adjusted to the VIRUS observations. This adjusted model agrees well with our radial profile at $r \lesssim 80$ kpc. At larger radii, our measured profile is flatter.

We also compared the radial profile with the median radial Lyα surface brightness profiles of galaxies with stellar masses of 10^8–$10^{11} M_\odot$ at $z = 3$, taken from the radiative transfer simulation of Byrohl et al. (2021). The simulation results agree well with our measurement at most radii, except at $r < 10$ kpc and 30 kpc $< r <$ 60 kpc. The comparison suggests that our surface brightness profile at $r \lesssim 100$ kpc is dominated by photons emitted in star-forming regions in the central galaxy, and at $r \gtrsim 100$ kpc, by photons from galaxies in other dark matter halos. A similar conclusion was reached in Kikuchihara et al. (2021).

Finally, we compared the radial profile with the prediction of Kakiichi & Dijkstra (2018) that the Lyα halo is proportional to $r^{-2.4}$ for $r > 20$ kpc. This power-law profile fits the measured radial profile well at $r \leqslant 80$ kpc. At larger radii, our measured profile is flatter. Because Kakiichi & Dijkstra (2018) only considered scattered photons from the central galaxy, this result further suggests that the flattening is due to photons originating from other dark matter halos.

The radiative transfer simulation of Byrohl et al. (2021) predicts that the median Lyα profiles of LAEs have similar shapes across redshifts, stellar masses, and luminosities. The similarity of the shapes of our median radial profile and that in Wisotzki et al. (2018), which are at higher redshifts and fainter than our sample, suggests that median Lyα profiles at small radii indeed have similar shapes between redshifts $2 < z < 4$ and across a factor of 10 in luminosity.

In conclusion, this measurement of faint Lyα surface brightness to >100 kpc from LAEs shows the high scientific potential of HETDEX observations. The methods for quantifying systematic uncertainties developed in this paper will be valuable for Lyα intensity mapping (Kovetz et al. 2017; Croft et al. 2018; Kakuma et al. 2021; Kikuchihara et al. 2021) with HETDEX, which will improve constraints on cosmological parameters.

We thank M. Gronke for useful discussions and F. Arrigoni Battaia for comments on the draft. We thank the referee for their helpful, constructive feedback. E.K.'s work was supported in part by the Deutsche Forschungsgemeinschaft (DFG, German Research Foundation) under Germany's Excellence Strategy—EXC-2094-390783311.

HETDEX is led by the University of Texas at Austin McDonald Observatory and Department of Astronomy with participation from the Ludwig-Maximilians-Universität München, Max-Planck-Institut für Extraterrestrische Physik (MPE), Leibniz-Institut für Astrophysik Potsdam (AIP), Texas A&M University, Pennsylvania State University, Institut für Astrophysik Göttingen, The University of Oxford, Max-Planck-Institut für Astrophysik (MPA), The University of Tokyo, and Missouri University of Science and Technology. In addition to Institutional support, HETDEX is funded by the National Science Foundation (grant AST-0926815), the State of Texas, the US Air Force (AFRL FA9451-04-2-0355), and generous support from private individuals and foundations.

The observations were obtained with the Hobby-Eberly Telescope (HET), which is a joint project of the University of Texas at Austin, the Pennsylvania State University, Ludwig-Maximilians-Universität München, and Georg-August-Universität Göttingen. The HET is named in honor of its principal benefactors, William P. Hobby and Robert E. Eberly.

VIRUS is a joint project of the University of Texas at Austin, Leibniz-Institut für Astrophysik Potsdam (AIP), Texas A&M University (TAMU), Max-Planck-Institut für Extraterrestrische Physik (MPE), Ludwig-Maximilians-Universität München, Pennsylvania State University, Institut für Astrophysik Göttingen, University of Oxford, Max-Planck-Institut für Astrophysik (MPA), and The University of Tokyo.

The authors acknowledge the Texas Advanced Computing Center (TACC) at The University of Texas at Austin for providing high performance computing, visualization, and

storage resources that have contributed to the research results reported within this paper. URL: http://www.tacc.utexas.edu.

The Kavli IPMU is supported by World Premier International Research Center Initiative (WPI), MEXT, Japan. The Institute for Gravitation and the Cosmos is supported by the Eberly College of Science and the Office of the Senior Vice President for Research at Pennsylvania State University.

This research made use of NASA's Astrophysics Data System Bibliographic Services.

This research has made use of the VizieR catalog access tool, CDS, Strasbourg, France. The original description of the VizieR service was published in A&AS 143, 23.

This research made use of Astropy,[15] a community-developed core Python package for Astronomy (Astropy Collaboration et al. 2013, 2018), Matplotlib (Hunter 2007), Numpy (Harris et al. 2020), and Scipy (Virtanen et al. 2020).

Facility: The Hobby-Eberly Telescope (McDonald Observatory)

ORCID iDs

Maja Lujan Niemeyer https://orcid.org/0000-0002-6907-8370
Eiichiro Komatsu https://orcid.org/0000-0002-0136-2404
Chris Byrohl https://orcid.org/0000-0002-0885-8090
Dustin Davis https://orcid.org/0000-0002-8925-9769
Maximilian Fabricius https://orcid.org/0000-0002-7025-6058
Karl Gebhardt https://orcid.org/0000-0002-8433-8185
Gary J. Hill https://orcid.org/0000-0001-6717-7685
Lutz Wisotzki https://orcid.org/0000-0003-2977-423X
William P. Bowman https://orcid.org/0000-0003-4381-5245
Robin Ciardullo https://orcid.org/0000-0002-1328-0211
Daniel J. Farrow https://orcid.org/0000-0003-2575-0652
Steven L. Finkelstein https://orcid.org/0000-0001-8519-1130
Eric Gawiser https://orcid.org/0000-0003-1530-8713
Caryl Gronwall https://orcid.org/0000-0001-6842-2371
Donghui Jeong https://orcid.org/0000-0002-8434-979X
Martin Landriau https://orcid.org/0000-0003-1838-8528
Chenxu Liu https://orcid.org/0000-0001-5561-2010
Erin Mentuch Cooper https://orcid.org/0000-0002-2307-0146
Masami Ouchi https://orcid.org/0000-0002-1049-6658
Donald P. Schneider https://orcid.org/0000-0001-7240-7449
Gregory R. Zeimann https://orcid.org/0000-0003-2307-0629

References

Arrigoni Battaia, F., Hennawi, J. F., Cantalupo, S., & Prochaska, J. X. 2016, ApJ, 829, 3
Arrigoni Battaia, F., Hennawi, J. F., Prochaska, J. X., et al. 2019a, MNRAS, 482, 3162
Arrigoni Battaia, F., Obreja, A., Prochaska, J. X., et al. 2019b, A&A, 631, A18
Astropy Collaboration, Robitaille, T. P., Tollerud, E. J., et al. 2013, A&A, 558, A33
Astropy Collaboration, Price-Whelan, A. M., Sipőcz, B. M., et al. 2018, AJ, 156, 123
Bacon, R., Accardo, M., Adjali, L., et al. 2010, Proc. SPIE, 7735, 773508
Bacon, R., Mary, D., Garel, T., et al. 2021, A&A, 647, A107
Beers, T. C., Flynn, K., & Gebhardt, K. 1990, AJ, 100, 32
Bond, N. A., Feldmeier, J. J., Matković, A., et al. 2010, ApJL, 716, L200
Borisova, E., Cantalupo, S., Lilly, S. J., et al. 2016, ApJ, 831, 39
Byrohl, C., Nelson, D., Behrens, C., et al. 2021, MNRAS, 506, 5129
Cai, Z., Fan, X., Yang, Y., et al. 2017, ApJ, 837, 71
Cai, Z., Hamden, E., Matuszewski, M., et al. 2018, ApJL, 861, L3
Cai, Z., Cantalupo, S., Prochaska, J. X., et al. 2019, ApJS, 245, 23
Camps, P., Behrens, C., Baes, M., Kapoor, A. U., & Grand, R. 2021, ApJ, 916, 39
Cantalupo, S., Arrigoni-Battaia, F., Prochaska, J. X., Hennawi, J. F., & Madau, P. 2014, Natur, 506, 63
Cantalupo, S., Porciani, C., Lilly, S. J., & Miniati, F. 2005, ApJ, 628, 61
Christensen, L., Jahnke, K., Wisotzki, L., & Sánchez, S. F. 2006, A&A, 459, 717
Ciardullo, R., Gronwall, C., Adams, J. J., et al. 2013, ApJ, 769, 83
Claeyssens, A., Richard, J., Blaizot, J., et al. 2019, MNRAS, 489, 5022
Claeyssens, A., Richard, J., Blaizot, J., et al. 2022, arXiv:2201.04674
Croft, R. A. C., Miralda-Escudé, J., Zheng, Z., Blomqvist, M., & Pieri, M. 2018, MNRAS, 481, 1320
Croft, R. A. C., Miralda-Escudé, J., Zheng, Z., et al. 2016, MNRAS, 457, 3541
Dijkstra, M. 2019, Physics of Lyα Radiative Transfer, Vol. 46 (Berlin: Springer-Verlag), 1
Dijkstra, M., & Kramer, R. 2012, MNRAS, 424, 1672
Erb, D. K., Steidel, C. C., & Chen, Y. 2018, ApJL, 862, L10
Fardal, M. A., Katz, N., Gardner, J. P., et al. 2001, ApJ, 562, 605
Farina, E. P., Arrigoni-Battaia, F., Costa, T., et al. 2019, ApJ, 887, 196
Farrow, D. J., Sánchez, A. G., Ciardullo, R., et al. 2021, MNRAS, 507, 3187
Faucher-Giguère, C.-A., Kereš, D., Dijkstra, M., Hernquist, L., & Zaldarriaga, M. 2010, ApJ, 725, 633
Feldmeier, J. J., Hagen, A., Ciardullo, R., et al. 2013, ApJ, 776, 75
Feltre, A., Maseda, M. V., Bacon, R., et al. 2020, A&A, 641, A118
Fossati, M., Fumagalli, M., Lofthouse, E. K., et al. 2021, MNRAS, 503, 3044
Gaia Collaboration, Brown, A. G. A., Vallenari, A., et al. 2016, A&A, 595, A2
Gallego, S. G., Cantalupo, S., Lilly, S., et al. 2018, MNRAS, 475, 3854
Gallego, S. G., Cantalupo, S., Sarpas, S., et al. 2021, MNRAS, 504, 16
Gebhardt, K., Mentuch Cooper, E., Ciardullo, R., et al. 2021, ApJ, 923, 217
Goto, T., Utsumi, Y., Furusawa, H., Miyazaki, S., & Komiyama, Y. 2009, MNRAS, 400, 843
Gould, A., & Weinberg, D. H. 1996, ApJ, 468, 462
Gronke, M., & Bird, S. 2017, ApJ, 835, 207
Haiman, Z., Spaans, M., & Quataert, E. 2000, ApJL, 537, L5
Harris, C. R., Millman, K. J., van der Walt, S. J., et al. 2020, Natur, 585, 357
Hayashino, T., Matsuda, Y., Tamura, H., et al. 2004, AJ, 128, 2073
Hayes, M., Östlin, G., Mas-Hesse, J. M., et al. 2005, A&A, 438, 71
Hayes, M., Östlin, G., Schaerer, D., et al. 2013, ApJL, 765, L27
Hayes, M., Östlin, G., Duval, F., et al. 2014, ApJ, 782, 6
Hennawi, J. F., Prochaska, J. X., Cantalupo, S., & Arrigoni-Battaia, F. 2015, Sci, 348, 779
Hill, G. J., Gebhardt, K., Komatsu, E., et al. 2008, in ASP Conf. Ser. 399, The Hobby-Eberly Telescope Dark Energy Experiment (HETDEX): Description and Early Pilot Survey Results, ed. T. Kodama, T. Yamada, & K. Aoki (San Francisco, CA: ASP), 115
Hill, G. J., Lee, H., MacQueen, P. J., et al. 2021, AJ, 162, 298
Huang, Y., Lee, K.-S., Shi, K., et al. 2021, ApJ, 921, 4
Hunter, J. D. 2007, CSE, 9, 90
Jiang, L., Egami, E., Fan, X., et al. 2013, ApJ, 773, 153
Kakiichi, K., & Dijkstra, M. 2018, MNRAS, 480, 5140
Kakuma, R., Ouchi, M., Harikane, Y., et al. 2021, ApJ, 916, 22
Kikuchihara, S., Harikane, Y., Ouchi, M., et al. 2021, arXiv:2108.09288
Kikuta, S., Matsuda, Y., Cen, R., et al. 2019, PASJ, 71, L2
Kimock, B., Narayanan, D., Smith, A., et al. 2021, ApJ, 909, 119
Kollmeier, J. A., Zheng, Z., Davé, R., et al. 2010, ApJ, 708, 1048
Kovetz, E. D., Viero, M. P., Lidz, A., et al. 2017, arXiv:1709.09066
Kusakabe, H., Verhamme, A., Blaizot, J., et al. 2022, arXiv:2201.07257
Lake, E., Zheng, Z., Cen, R., et al. 2015, ApJ, 806, 46
Leclercq, F., Bacon, R., Wisotzki, L., et al. 2017, A&A, 608, A8
Leclercq, F., Bacon, R., Verhamme, A., et al. 2020, A&A, 635, A82
Leung, A. S., Acquaviva, V., Gawiser, E., et al. 2017, ApJ, 843, 130
Martin, D. C., Chang, D., Matuszewski, M., et al. 2014a, ApJ, 786, 106
Martin, D. C., Chang, D., Matuszewski, M., et al. 2014b, ApJ, 786, 107
Mas-Ribas, L., & Dijkstra, M. 2016, ApJ, 822, 84
Mas-Ribas, L., Dijkstra, M., Hennawi, J. F., et al. 2017, ApJ, 841, 19
Matsuda, Y., Yamada, T., Hayashino, T., et al. 2004, AJ, 128, 569
Matsuda, Y., Yamada, T., Hayashino, T., et al. 2011, MNRAS, 410, L13
Matsuda, Y., Yamada, T., Hayashino, T., et al. 2012, MNRAS, 425, 878
McCarthy, P. J., Spinrad, H., Djorgovski, S., et al. 1987, ApJL, 319, L39

[15] http://www.astropy.org

Mitchell, P. D., Blaizot, J., Cadiou, C., et al. 2021, MNRAS, 501, 5757
Møller, P., & Warren, S. J. 1998, MNRAS, 299, 661
Momose, R., Ouchi, M., Nakajima, K., et al. 2014, MNRAS, 442, 110
Momose, R., Ouchi, M., Nakajima, K., et al. 2016, MNRAS, 457, 2318
Nakajima, K., Schaerer, D., Le Fèvre, O., et al. 2018, A&A, 612, A94
Nelson, D., Sharma, P., Pillepich, A., et al. 2020, MNRAS, 498, 2391
Östlin, G., Hayes, M., Kunth, D., et al. 2009, AJ, 138, 923
O'Sullivan, D. B., Martin, C., Matuszewski, M., et al. 2020, ApJ, 894, 3
Ouchi, M., Ono, Y., Egami, E., et al. 2009, ApJ, 696, 1164
Overzier, R. A., Röttgering, H. J. A., Kurk, J. D., & De Breuck, C. 2001, A&A, 367, L5
Patrício, V., Richard, J., Verhamme, A., et al. 2016, MNRAS, 456, 4191
Planck Collaboration, Aghanim, N., Akrami, Y., et al. 2020, A&A, 641, A6
Ramsey, L. W., Sebring, T. A., & Sneden, C. A. 1994, Proc. SPIE, 2199, 31
Rasekh, A., Melinder, J., Östlin, G., et al. 2021, arXiv:2110.01626
Rauch, M., Haehnelt, M., Bunker, A., et al. 2008, ApJ, 681, 856
Reuland, M., van Breugel, W., Röttgering, H., et al. 2003, ApJ, 592, 755
Runnholm, A., Hayes, M., Melinder, J., et al. 2020, ApJ, 892, 48
Santos, S., Sobral, D., Matthee, J., et al. 2020, MNRAS, 493, 141
Shibuya, T., Ouchi, M., Konno, A., et al. 2018, PASJ, 70, S14
Smit, R., Swinbank, A. M., Massey, R., et al. 2017, MNRAS, 467, 3306
Smith, D. J. B., & Jarvis, M. J. 2007, MNRAS, 378, L49
Smith, D. J. B., Jarvis, M. J., Lacy, M., & Martínez-Sansigre, A. 2008, MNRAS, 389, 799
Smith, D. J. B., Jarvis, M. J., Simpson, C., & Martínez-Sansigre, A. 2009, MNRAS, 393, 309
Spinoso, D., Orsi, A., López-Sanjuan, C., et al. 2020, A&A, 643, A149
Steidel, C. C., Adelberger, K. L., Shapley, A. E., et al. 2000, ApJ, 532, 170
Steidel, C. C., Bogosavljević, M., Shapley, A. E., et al. 2011, ApJ, 736, 160
Swinbank, A. M., Bower, R. G., Smith, G. P., et al. 2007, MNRAS, 376, 479
Umehata, H., Fumagalli, M., Smail, I., et al. 2019, Sci, 366, 97
van de Voort, F., Springel, V., Mandelker, N., van den Bosch, F. C., & Pakmor, R. 2019, MNRAS, 482, L85
van Ojik, R., Roettgering, H. J. A., Miley, G. K., & Hunstead, R. W. 1997, A&A, 317, 358
Virtanen, P., Gommers, R., Oliphant, T. E., et al. 2020, NatMe, 17, 261
Weidinger, M., Møller, P., & Fynbo, J. P. U. 2004, Natur, 430, 999
Weidinger, M., Møller, P., Fynbo, J. P. U., & Thomsen, B. 2005, A&A, 436, 825
Wisotzki, L., Bacon, R., Blaizot, J., et al. 2016, A&A, 587, A98
Wisotzki, L., Bacon, R., Brinchmann, J., et al. 2018, Natur, 562, 229
Wu, J., Jiang, L., & Ning, Y. 2020, ApJ, 891, 105
Xue, R., Lee, K.-S., Dey, A., et al. 2017, ApJ, 837, 172
Yang, Y., Zabludoff, A., Eisenstein, D., & Davé, R. 2010, ApJ, 719, 1654
Zhang, H., Ouchi, M., Itoh, R., et al. 2020, ApJ, 891, 177
Zhang, Y., Ouchi, M., Gebhardt, K., et al. 2021, ApJ, 922, 167
Zheng, Z., Cen, R., Weinberg, D., Trac, H., & Miralda-Escudé, J. 2011, ApJ, 739, 62